

A Spatial-Spectral-Frequency Interactive Network for Multimodal Remote Sensing Classification

Hao Liu^a, Yunhao Gao^{b,c}, Wei Li^{b,c}, Mingyang Zhang^{d,e}, Maoguo Gong^{d,e,f}, Lorenzo Bruzzone^{a,*}

^a*Department of Information Engineering and Computer Science, University of Trento, 38123 Trento, Italy*

^b*School of Information and Electronics, Beijing Institute of Technology, Beijing 100081, China*

^c*Beijing Key Laboratory of Fractional Signals and Systems, Beijing Institute of Technology, Beijing 100081, China*

^d*School of Electronic Engineering, Xidian University, Xi'an 710071, China*

^e*Key Laboratory of Collaborative Intelligent Systems of Ministry of Education, Xidian University, Xi'an 710071, China*

^f*Academy of Artificial Intelligence, Inner Mongolia Normal University, Hohhot 010028, China*

Abstract

Deep learning-based methods have achieved significant success in remote sensing Earth observation data analysis. Numerous feature fusion techniques address multimodal remote sensing image classification by integrating global and local features. However, these techniques often struggle to extract structural and detail features from heterogeneous and redundant multimodal images. With the goal of introducing frequency domain learning to model key and sparse detail features, this paper introduces the spatial-spectral-frequency interaction network (S²Fin), which integrates pairwise fusion modules across the spatial, spectral, and frequency domains. Specifically, we propose a high-frequency sparse enhancement transformer that employs sparse spatial-spectral attention to optimize the parameters of the high-frequency filter. Subsequently, a two-level spatial-frequency fusion strategy is introduced, comprising an adaptive frequency channel module that fuses low-frequency structures with enhanced high-frequency details, and a high-frequency resonance mask that emphasizes sharp edges via phase similarity. In addition, a spatial-spectral attention fusion module fur-

^{*}Corresponding author: Lorenzo Bruzzone (lorenzo.bruzzone@unitn.it)

ther enhances feature extraction at intermediate layers of the network. Experiments on four benchmark multimodal datasets with limited labeled data demonstrate that S²Fin performs superior classification, outperforming state-of-the-art methods. The code is available at <https://github.com/HaoLiu-XDU/SSFin>.

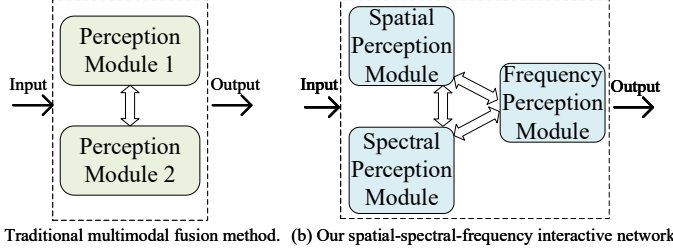
Keywords: Multimodal fusion, frequency domain, hyperspectral and multispectral images, deep learning, remote sensing.

1. Introduction

Classification of remote sensing imagery enables extraction of Earth-surface information for applications such as environmental monitoring [1], urban planning [2], and natural-resource management [3].

Hyperspectral images (HSIs) and multispectral images (MSIs) produce spatial-spectral data cubes but are sensitive to atmospheric conditions [4]. Synthetic aperture radar (SAR) offers all-weather imaging but introduces speckle noise, while light detection and ranging (LiDAR) provides high-resolution elevation data yet has limited penetration in vegetation and poorer performance in adverse weather [5, 6]. Fusing spectral and active sensor data exploits their complementary strengths to improve classification accuracy and robustness in remote sensing applications [7, 8].

Recently, deep learning-based methods have emerged as promising tools for spectral and active sensor data classification [9]. Methods fall into two categories: 1) those that extract spatial information and 2) those that jointly exploit spatial-spectral features. Because multimodal data provide abundant spatial information, many spatial fusion-based methods have been proposed, including reconstruction-based methods [10, 11], adversarial training strategies [12], representation enhancement approaches [13], and self-supervised learning techniques [14]. However, these methods often do not fully exploit the information in the image spectral domain, resulting in reduced classification accuracy. Many studies have focused on spatial-spectral fusion techniques for multimodal remote sensing classification, including two-branch CNN



(a) Traditional multimodal fusion method. (b) Our spatial-spectral-frequency interactive network.

Figure 1: Workflow comparisons. (a) The interaction and fusion of networks 1 and 2 usually focus on two of the spatial, spectral, and frequency domains. (b) The proposed S²Fin aims to enhance the interaction between the three domains and different levels of the network.

frameworks [15], spectral sequence transformers [16], masked autoencoders [17], and global-local fusion networks [18, 19]. These methods obtain good results in multimodal classification. However, Chen et al. [20] observed that the fused multimodal features often show intra-category inconsistency and boundary displacement. These problems restrict accurate pixel-level classification, especially when few labeled samples are available.

In real-world remote sensing scenarios, obtaining labels is both time and labor intensive [21]. How to extract effective feature and obtain accurate classification with limited samples is still an open challenge. In this context, spatial-frequency domain techniques offer a promising solution by inherently generating sparse representations that emphasize high-frequency components. These components capture critical details such as edges and textures [22, 23], which are essential for distinguishing similar categories. By focusing on these high-quality discriminative features, frequency domain learning reduces the reliance on large training datasets. In addition, since spatial frequency domain methods can improve spatial modeling from a global perspective [24], spatial-frequency fusion can be used to improve image processing tasks [25]. In the field of remote sensing, research has focused on Fourier transform-based methods [26, 27], fractional fusion techniques [28–30] and Gabor filter-based feature extraction approaches [31]. As illustrated in Fig. 1(a), previous methods mainly observe and fuse multimodal information from two domains, without explicitly integrating

spatial–spectral–frequency information.

Although recent advancements in multimodal image classification have yielded significant improvements, significant limitations still exists: 1) High similarity and continuity among spectral bands in hyperspectral images result in difficulty for extracting optimal features. Previous studies have largely overlooked the decomposition of spectral signals, focusing instead on methods to extract complex and redundant features. 2) High- and low-level network features correspond to object-level semantics and fine-grained background textures, respectively. Correspondingly, low-frequency components effectively encode global structure and semantics, whereas high-frequency components capture fine details [32]. However, few studies have emphasized enhancing the frequency components in shallow and deep network layers to improve feature extraction.

To address these challenges, this paper introduces a spatial-spectral-frequency interaction network (S^2Fin), which includes pairwise fusion modules for the three considered domains as shown in Fig. 1(b). Initially, the high-frequency sparse enhancement transformer (HFSET) is developed to utilize sparse spatial-spectral attention to optimize the parameters of the high-frequency filter, thereby amplifying critical high-frequency signal components. Meanwhile, the adaptive frequency channel module (AFCM) enhances the high-frequency channels of multimodal images while integrating low-frequency channels, thereby amplifying modality-specific details and fusing shared structural features. Subsequently, spectral-spatial features from spectral images undergo spectral-spatial attention fusion (SSAF) and Mamba blocks, which are further combined with active sensor data. Then a high-frequency resonance mask (HFRM) is applied to enhance feature representation at critical image locations. Finally, the features from all fusion modules are integrated to achieve multimodal classification.

The main contributions in this paper can be highlighted as follows.

1. We propose S^2Fin , a novel multimodal remote sensing classification framework,

integrating pairwise fusion and frequency enhancement modules across spatial, spectral, and frequency domains.

2. We introduce the HFSET to extract key spectral features. This module employs a sparse spatial-spectral attention mechanism to improve the estimation of high-frequency filter’s parameters, thereby enabling discriminative spectral frequency refinement.
3. We present a two-level spatial-frequency fusion strategy utilizing the AFCM and HFRM in shallow and deep network layers, respectively. The AFCM fuses low-frequency structural information and enhances high-frequency modality-specific details by balancing channel attention. The HFRM amplifies specific amplitude regions based on phase similarity, strengthening the focus on modality-common areas.

The remainder of this paper is organized as follows. Section 2 provides background knowledge about S²Fin. Section 3 describes the proposed method. Section 4 validates the effectiveness of S²Fin on four remote sensing datasets and analyzes the related hyperparameters. Finally, Section 5 draws the conclusions of this paper.

2. Related Work

This section first reviews the background and advanced methods of frequency domain learning, then introduces related techniques of multimodal feature fusion.

2.1. High-Frequency Enhancement

Frequency domain transformations are widely used methodology for converting signals from their original temporal or spatial representations into a form that expresses frequency components [32, 33]. Frequency domain transform can analyze the amplitude, phase, and frequency distribution of a signal to achieve the various tasks including filtering, noise reduction, and feature extraction [25, 26, 28, 34].

In the spatial frequency domain of an image, low-frequency components typically correspond to the smooth areas, whereas high-frequency components correspond to the rapidly changing parts, such as edges, textures, and details [22]. In the literature, several techniques focused on the high-frequency enhancement to extract key features. Sun et al. [35] utilized an high-frequency enhancement module to capture details present in the images. Behjati et al. [36] proposed a frequency-based enhancement block to enhance the part of high frequencies while forward the low-frequencies. Wang et al. [37] employed fast Fourier convolution with attention mechanism in the high-frequency domain.

In the frequency domain, phase information describes the position and structure of the various frequency components within an image. It encodes the relative positions of different frequency components, serving as a key carrier of image structural information [33]. This work aims to utilize high-frequency enhancement methods and phase information to build spatial mask for multimodal feature extraction.

2.2. *Multimodal Image Classification*

Multimodal learning integrates complementary information from different data sources, resulting in robust and reliable outcomes in various tasks. In remote sensing data classification, deep learning multimodal architectures, primarily based on CNNs and Transformers, are increasingly popular.

CNNs effectively capture local features and are widely used for multimodal data fusion. For example, Wu et al. [11] introduced a CNN backbone with a cross-channel reconstruction module, while Gao et al. [12] proposed an adversarial complementary learning strategy within a CNN model. Wang et al. [13] developed a representation-enhanced status replay network. However, although these techniques excel at detecting local features, their strong local sensitivity and lack of long-range dependency modeling limit their ability to capture rich contextual information.

Due to its powerful global perception, the Transformer has recently been applied

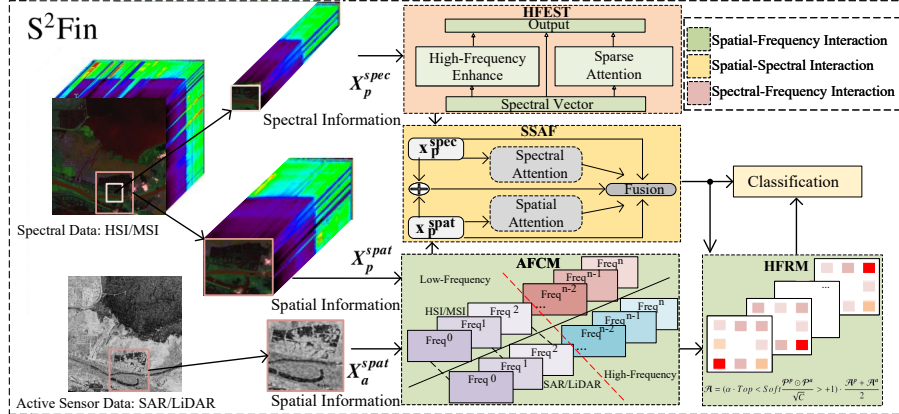


Figure 2: Illustration of the proposed S^2Fin framework.

to the fusion of multimodal remote sensing imagery. For instance, Xue et al. [16] proposed a deep hierarchical vision Transformer, and Zhou et al. [38] employed a four-branch deep feature extraction framework with a dynamic multi-scale feature extraction module for multimodal joint classification, while Ni et al. [39] introduced a multiscale head selection Transformer.

Recently, Mamba has attracted attention for multimodal fusion because of its efficient training and inference capabilities [40]. In the field of remote sensing, there are studies on spatial-spectral Mamba [41] and multi-scale Mamba [42]. The Mamba architecture uses the state space model to capture long-range dependencies, which reduces computational requirements and is suitable for long sequence tasks [43]. Meanwhile, the transformer focuses on global features based on the attention mechanism. This work fuse multimodal data based on Mamba and transformer techniques to achieve long-range dependency feature fusion and save computing resources..

3. Methodology

S^2Fin is designed to achieve accurate classification with few-labeled samples by interactively extracting key multimodal information. Fig. 2 depicts the comprehensive

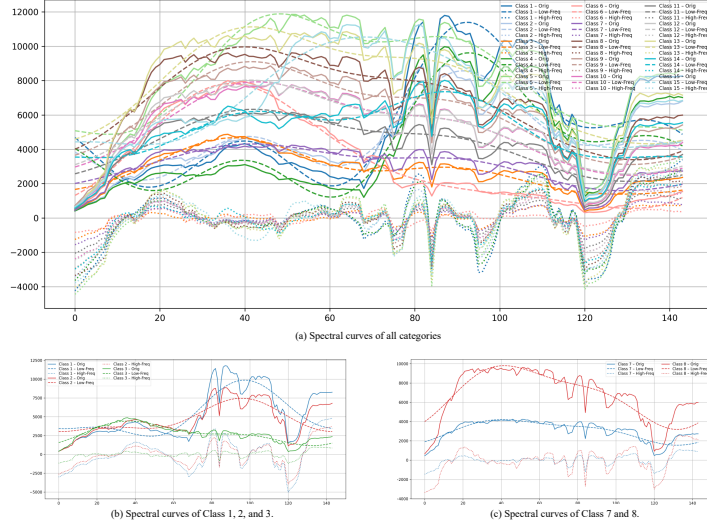


Figure 3: Spectral curves filtered by low- and high-frequency components of the HSI of the Houston dataset obtained via 1D discrete Fourier transform. The horizontal axis represents the number of bands and the vertical axis represents the reflectivity values. (a) All categories. (b) Categories 1 (healthy grass), 2 (stressed grass), and 3 (synthetic grass). (c) Categories 7 (residential) and 8 (commercial).

framework of S²Fin, which implements pairwise fusion of spatial, spectral, and frequency domains. These interactive modules include HFSET for spectral-frequency fusion, AFCM and HFRM for two-level spatial-frequency fusion, and SSAF for spatial-spectral fusion at the middle level of the network. These modules aim to enhance the high-frequency detail components and inter-domain interaction. The inputs to S²Fin are the spectral data patch X_p^{spec} and spatial data patch X_p^{spat} of spectral images (HSI or MSI), as well as the spatial data patch X_a^{spat} of active remote sensing data (SAR or LiDAR).

In the next subsections, the modules included in the S²Fin framework are described in detail, offering insights into their functionalities.

3.1. High-Frequency Enhancement and Sparse Transformer

Remote sensing objects exhibit spectral signatures that are both complex and closely similar, making it challenging to characterize their spectral-dimensional features. Frequency-domain analysis decomposes a spectral signal into low-frequency

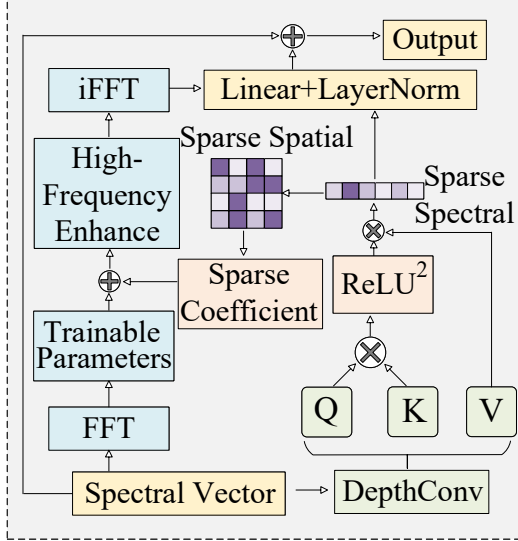


Figure 4: Structure of HFSET. The left part represents the high-frequency enhancement branch, while the right part is the sparse attention branch. The two branches are merged through a linear layer and a norm layer.

components, which are smooth and highly correlated, and high-frequency components that exhibit larger variations. As illustrated in Fig. 3, a simple 1D discrete Fourier transform (DFT) reveals that low-frequency components of remote sensing images substantially overlap and are difficult to distinguish, whereas high-frequency components display distinct inter-class variation. Figs. 3(b)-(c) compare specific categories, highlighting this disparity more clearly.

Motivated by these observations, the HFSET mainly utilizes a sparse spatial-spectral attention to enhance the high-frequency filter’s parameters, as shown in the Fig. 4. Initially, HSI and MSI have multiple spectral channels, which especially in HSI may have high similarity and redundancy. We combine depth-wise convolution and squared ReLU-based attention to remove the similarities with negative relevance from the spectral dimension.

First, we obtain the Q , K , and V required for attention through depth-wise convolution, which captures spectral relationships within individual channels:

$$\mathbf{Q}, \mathbf{K}, \mathbf{V} = \text{split}(\text{Depth-Conv}(X_p^{spec})), \quad (1)$$

where *split* divides the depth-wise convolution tensor into attention vectors. The spectral features $\mathbf{x}_{sparse}^{spec}$ after sparse attention processing can be expressed as:

$$\mathbf{x}_{sparse}^{spec} = \text{ReLU}^2(\mathbf{Q}\mathbf{K}^\top) \cdot \mathbf{V}, \quad (2)$$

where ReLU^2 represents squared ReLU activation function.

After spectral sparse attention, spatial sparse attention is performed to generate guidance for frequency domain enhancement coefficients. Specifically, in the spatial domain, M vectors are arranged in descending order, forming the sequence $\mathbf{z} = [z_{(1)}, z_{(2)}, \dots, z_{(M)}]$. Subsequently, the parameter \hat{m} is determined as follows:

$$\begin{aligned} S_m &= \sum_{j=1}^m z_{(j)}, \quad \text{for } m = 1, 2, \dots, M \\ \hat{m} &= \max \left\{ m \in \{1, \dots, M\} : z_{(m)} > \frac{S_m - 1}{m} \right\}, \end{aligned} \quad (3)$$

where S_m denotes the cumulative sum of the top m elements. Based on \hat{m} , the sparse threshold τ is then computed as:

$$\tau = \frac{S_{\hat{m}} - 1}{\hat{m}} \quad (4)$$

Elements falling below this threshold are set to zero, resulting in the sparse coefficient weight \mathbf{w} as defined in Eq. (5). Furthermore, we work on the high-frequency enhancement branch. The trainable thresholds f_{cutoff} and gain coefficients g_{amp} are added to the transform, and the values are automatically updated as the network iter-

ates. This process can be expressed as:

$$\mathcal{F}'(X_p^{spec}) = \begin{cases} 0, & \text{if } |f| < f_{\text{cutoff}} \\ \mathcal{F}(X_p^{spec}) \cdot g_{\text{amp}} \cdot (w + 1), & \text{otherwise} \end{cases} \quad (5)$$

where \mathcal{F} and f are the Fourier transform and frequency component, respectively. After inverse Fourier transform \mathcal{F}'^{-1} , we can get the enhanced high-frequency components x_{hf}^{spec} . The output of the HFSET is obtained as:

$$x_p^{spec} = FC \cdot (x_{sparse}^{spec}, x_{hf}^{spec})) + X_p^{spec}, \quad (6)$$

where FC represents a linear layer.

3.2. Two-Level Spatial-Frequency Fusion

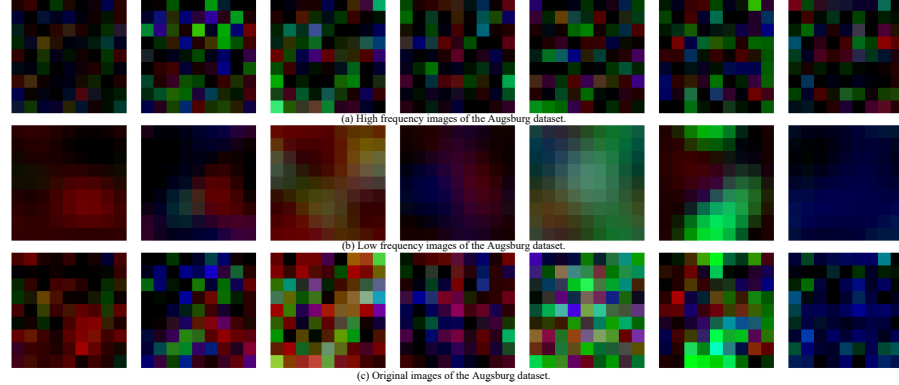


Figure 5: Example of images of the HSIs of the Augsburg dataset filtered by low- and high-frequency components obtained by applying a 2D DFT along the spatial dimension. Three main bands are selected following principal component analysis (PCA), and ten samples per class are processed by DFT to generate average component magnitude images. The seven class-averaged images are displayed from left to right.

The two-level spatial-frequency fusion strategy is designed to separately extract semantic category information and boundary details from different network layers [20]. As illustrated in Fig. 5, low-frequency components typically capture the structural information of ground objects, whereas high-frequency components encode fine-

grained category-specific details. This strategy incorporates the AFCM module for low-level channel attention and the HFRM module for high-level spatial amplitude resonance.

3.2.1. Adaptive Frequency Channel Module

A fundamental step in our methodology is the transformation of spatial features into the frequency domain to enable feature recalibration based on frequency content. To this end, we employ the regularized 2D discrete cosine transform (DCT), formally defined for a single-channel input $\mathbf{x} \in \mathbb{R}^{H \times W}$ as:

$$\mathbf{f}_{h,w}^{Fre} = C(h) \cdot C(w) \sum_{i=0}^{H-1} \sum_{j=0}^{W-1} \mathbf{x}_{i,j} \cos\left(\frac{\pi h}{H}\left(i + \frac{1}{2}\right)\right) \cos\left(\frac{\pi w}{W}\left(j + \frac{1}{2}\right)\right), \quad (7)$$

$$s.t. \quad h \in \{0, 1, \dots, H-1\}, w \in \{0, 1, \dots, W-1\},$$

where $\mathbf{f}^{Fre} \in \mathbb{R}^{H \times W}$ is the resulting frequency spectrum. The normalization coefficients $C(u)$ are given by $C(u) = \sqrt{1/N}$ for $u = 0$ and $C(u) = \sqrt{2/N}$ for $u > 0$, where N represents the length of the dimension. This ensures the orthogonality of the transform.

The central motivation of the AFCM is that the frequency spectrum can be partitioned to disentangle shared, structural information from modality-specific details. Low-frequency coefficients encode global structure and are amenable to joint cross-modal processing, whereas high-frequency coefficients capture fine texture and should be preserved modality-specifically to retain unique characteristics.

This principle is mathematically realized as follows. Given two multimodal spatial feature maps, \mathbf{X}_p^{spat} and \mathbf{X}_a^{spat} , corresponding to spectral and active sensor data, the modulated output \mathbf{x}_p^{spat} for the passive modality is computed by:

$$\begin{aligned} \mathbf{x}_p^{spat} = \mathbf{X}_p^{spat} \odot & \left(\sigma \cdot FC(\mathcal{P}_{high}(\text{DCT}(\mathbf{X}_p^{spat}))) \right. \\ & \left. + \sigma \cdot FC\left(\frac{\mathcal{P}_{low}(\text{DCT}(\mathbf{X}_p^{spat})) + \mathcal{P}_{low}(\text{DCT}(\mathbf{X}_a^{spat}))}{2}\right) + 1 \right), \end{aligned} \quad (8)$$

where \odot denotes the element-wise Hadamard product. The operators $\mathcal{P}_{\text{low}}(\cdot)$ and $\mathcal{P}_{\text{high}}(\cdot)$ represent the frequency partitioning functions, which extract vectors of low- and high-frequency coefficients from a given spectrum based on predefined index sets. σ is the sigmoid activation function. The corresponding output for the active modality, $\mathbf{x}_a^{\text{spat}}$, is obtained through a symmetrical application of Eq. (8). This mechanism thereby allows the network to dynamically fuse shared structural knowledge while concurrently enhancing distinguishing modality-specific information.

3.2.2. High-Frequency Resonance Mask

On the one hand, to amplify the common information of multimodal images, we try to find the high-frequency regions of each modality as shown in Fig 5(a), and enhance these similar regions. On the other hand, the semantic information in the deep layers of the network is highly correlated with the classes to be recognized. The HFRM is designed to amplify the details feature.

The spatial features \mathbf{f}^s and $\mathbf{f}_a^{\text{spat}}$, namely the amplitude and phase of the spectral and active sensor data in this module, are obtained through Fourier transform:

$$\mathcal{A}^p, \mathcal{P}^p = \mathcal{F}(\mathbf{f}^s), \quad \mathcal{A}^a, \mathcal{P}^a = \mathcal{F}(\mathbf{f}_a^{\text{spat}}). \quad (9)$$

The amplitude represents the intensity of the various frequency components within an image. Enhancing the amplitude in the high-frequency areas improves the image's details and the edge features [22]. Intuitively, the HFGM locates the significant high-frequency parts within an image by leveraging the phase correlations of multimodal data, and subsequently enhances the image detail information by amplifying the amplitude.

The amplitude at this location with highest attention value is intensified:

$$\mathcal{A} = (\alpha \cdot \text{Top} < \text{Soft} \frac{\mathcal{P}^p \odot \mathcal{P}^a}{\sqrt{C}} > +1) \cdot \frac{\mathcal{A}^p + \mathcal{A}^a}{2}, \quad (10)$$

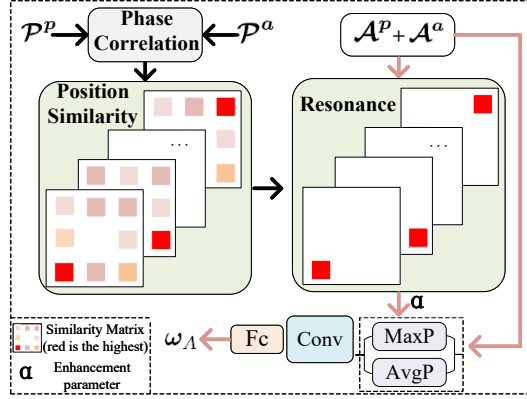


Figure 6: Illustration of the generation process of ω_A . First the operations with black arrows are applied, then the operations with red arrows are applied.

where C refers to the number of channels, and $Soft$ denotes the Softmax function. $Top < \cdot >$ selects the position with the highest similarity, \mathcal{A} represents the final integrated amplitude, and α is a trade-off parameter.

To further eliminate noise and extract high-level semantic information that is beneficial for classification, further processing of the amplitude is undertaken:

$$\omega_A = Soft \cdot FC \cdot Conv \cdot (MaxP(\mathcal{A}), AvgP(\mathcal{A})), \quad (11)$$

where $MaxP$ and $AvgP$ denote the operations of maximum and average pooling, respectively, and $Conv$ represents a two-dimensional convolution operation. The perception process of ω_A is depicted in Fig. 6, where different colors represent distinct spatial weight values, with the top used to select the positions of the highest values.

Finally, the resulting integrated amplitude and phase can be written as:

$$\begin{aligned} \mathcal{A}_{fusion} &= (1 + \omega_A) \cdot (\mathcal{A}^p + \mathcal{A}^a)/2, \\ \mathcal{P}_{fusion} &= Conv \cdot (\mathcal{P}^p + \mathcal{P}^a)/2. \end{aligned} \quad (12)$$

After inverse transform \mathcal{F}^{-1} , we can obtain the multimodal spatial features f^{spat} .

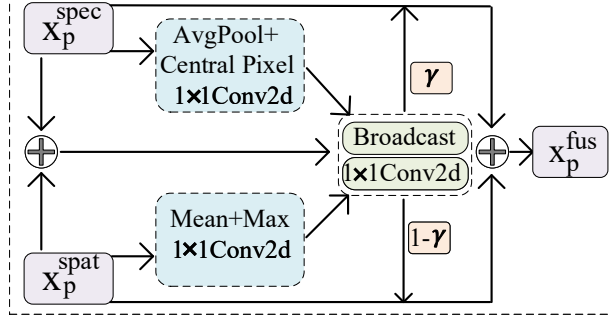


Figure 7: Flowchart of the proposed SSAF.

3.3. Spatial-Spectral Fusion

SSAF attempts to extend the spectral attention score obtained by HFSET to spatial data, while applies the attention score from AFCM, thereby synthesizing spatial-spectral interaction features. Fig. 7 shows the network structure.

With x_p^{spat} and x_p^{spec} in Eq. (8) as input, the integrated attention scores are:

$$\begin{aligned} Atte^{spat} &= \sigma \cdot Conv \cdot \left(\frac{1}{H \cdot W} \sum_{h=1}^H \sum_{w=1}^W x_p^{spat}, cent(x_p^{spat}) \right), \\ Atte^{spec} &= \sigma \cdot Conv \cdot \left(\frac{1}{C} \sum_{c=1}^C x_p^{spec}, \max_{c \in \{1, \dots, C\}} x_p^{spec} \right), \end{aligned} \quad (13)$$

where $cent$ represents the spatial center feature and $\max_{c \in \{1, \dots, C\}}$ represents the maximum spectral feature of the channel dimension. Then fused features and attention scores are:

$$\begin{aligned} x_p^{ss} &= x_p^{spat} + x_p^{spec}, \\ Atte^{fus} &= Broadcast(Atte^{spat}, Atte^{spec}), \end{aligned} \quad (14)$$

where $Broadcast$ expands the attention scores to the entire feature map along the

channel and spatial dimensions. Subsequently, the output of SSAF can be written as:

$$\begin{aligned}\gamma &= \sigma \cdot (\text{Conv} \cdot (\mathbf{x}_p^{ss}, \text{Atte}^{fus})), \\ \mathbf{x}_p^{fus} &= \sigma \cdot \text{Conv}(\mathbf{x}^{ss} + \gamma \cdot \mathbf{x}_p^{spec} + (1 - \gamma) \cdot \mathbf{x}_p^{spat}).\end{aligned}\tag{15}$$

Furthermore, we employ the Mamba module [40] to extract long-range dependency features f_p^{spat} and f_p^{fus} from \mathbf{x}_p^{spat} and \mathbf{x}_p^{fus} , respectively, and refine their fusion via an attention mechanism:

$$\begin{aligned}\mathbf{F}^{ss} &= \sigma \cdot FC \cdot (\text{cent}(f_p^{spat}) + \frac{1}{C} \sum_{c=1}^C f_p^{fus}), \\ f^s &= \mathbf{F}^{ss} \cdot f_p^{spat}, \\ f^{fus} &= \mathbf{F}^{ss} \cdot f_p^{fus},\end{aligned}\tag{16}$$

where f^s is used to obtain f^{spat} in HFRM, while f^{fus} is used for the classification together with the features output by the HFRM module.

4. Experimental Results and Discussion

In this section, the multimodal remote sensing datasets and the evaluation criteria to assess the performance of the proposed S²Fin are briefly introduced. Then the procedures for the estimation of the hyperparameter values and ablation experiments are presented. Finally, S²Fin is compared with other related advanced methods and results are discussed.

Comparisons have been done against a range of classic and advanced state-of-the-art multimodal remote sensing classification methods. These methods fall into four main groups. (1) Attention-based spectral–spatial fusion: approaches that learn where to attend across spectra and space to improve discrimination (FusAtNet [44]). (2) Modality-aware architectural fusion: network designs that account for different sensor properties or combine complementary backbones (AsyFFNet [5], Fusion-HCT

[6], MACN [18]). (3) Learning and alignment strategies: training schemes that align modalities or reinforce robustness via coupled learning and contrastive objectives (CALC [45], UACL [46]). (4) Multi-scale and global-local aggregation: methods that fuse information at multiple scales or explicitly combine global and local features to retain context and fine details (NCGLF [19], MSFMamba [42]).

4.1. Description of Datasets

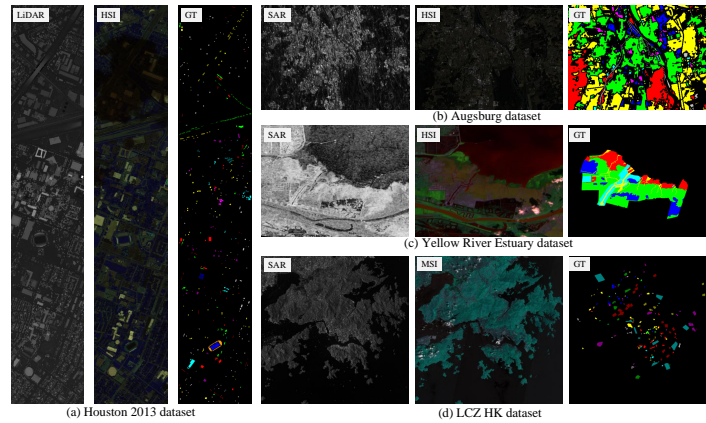


Figure 8: Multimodal remote sensing datasets. (a) Houston 2013 dataset. (b) Augsburg dataset. (c) Yellow River Estuary dataset. (d) LCZ HK dataset

Table 1: Land-cover classes and related numbers of samples in the four considered dataset.

Augsburg (HSI+SAR)			LCZ HK (MSI+SAR)			Houston 2013 (HSI+LiDAR)			
No.	Color	Name	No.	Color	Name	No.	Color	Name	
1	Red	Forest	1	Red	Compact High-rise	631	1	Red	Health Grass
2	Green	Residential Area	2	Green	Compact Mid-rise	179	2	Green	Stressed Grass
3	Blue	Industrial Area	3	Blue	Compact Low-rise	326	3	Blue	Synthetic Grass
4	Yellow	Low Plants	4	Yellow	Open High-rise	673	4	Yellow	Tress
5	Cyan	Allotment	5	Cyan	Open Mid-rise	126	5	Cyan	Soil
6	Magenta	Commercial Area	6	Magenta	Open Low-rise	120	6	Magenta	Water
7	Grey	Water	7	Grey	Large Low-rise	137	7	Grey	Residential
Total		78294	8	Grey	Heavy Industry	219	8	Grey	Commercial
Yellow River Estuary(HSI+SAR)			9	Red	Dense Trees	1616	9	Red	Road
1	Red	Spartina Alterniflora	10	Green	Scattered Trees	540	10	Green	Highway
2	Green	Stuenda Salsa	11	Green	Bush and Scrub	691	11	Green	Railway
3	Blue	Tamarix Forest	12	Purple	Low Plants	985	12	Purple	Parking Lot 1
4	Yellow	Tidal Creek	13	Cyan	Water	2603	13	Cyan	Parking Lot 2
5	Cyan	Mudflat	Total			8846	14	Blue	Tennis Court
Total		464671					15	Orange	Running Track
							Total	15029	

4.1.1. Houston 2013 dataset (HSI+LiDAR)

The Houston 2013 dataset, captured by the compact airborne spectrographic imager sensor in 2012 over the University of Houston, provides a detailed view of the urban campus and its surroundings. This dataset consists of HSI and LiDAR data, with each information source having a spatial resolution of 2.5 meters and dimensions of 349×1905 pixels. The HSI comprises 144 bands spanning the wavelength range from 0.38 to $1.05\mu\text{m}$, while the LiDAR data offer elevation measurements. The dataset is divided into the 15 distinct land-cover classes presented in Table 1 (a) together with the related numbers of labeled samples. A pseudo-color composite of the HSI and a grayscale image of the LiDAR data are displayed in Fig. 8, alongside the ground-truth map.

4.1.2. Augsburg dataset (HSI+SAR)

The Augsburg dataset is related to a detailed rural landscape near Augsburg, Germany. It consists of a 332×485 pixels hyperspectral image (HSI) and a SAR image. The HSI, captured by the HySpex sensor, covers 180 spectral bands from 400nm to 2500nm with a 30m ground sampling distance. The SAR image, obtained by the Sentinel-1 satellite and preprocessed by the European Space Agency using the sentinel application platform, includes dual-polarization (VV-VH) and single look complex (SLC) formats. The data set includes seven land-cover classes represented at a 30 m resolution. Fig. 8 (b) shows the pseudo-color composites of the HSI and SAR data, along with a ground truth map. Table 1 provides an overview of the classes and the related samples in the dataset.

4.1.3. Yellow River Estuary dataset (HSI+SAR)

The Yellow River Estuary dataset [3] offers a detailed perspective on the wetland scenes in Shandong Province, China. This region, known for its diverse landscapes and predominant herbaceous vegetation, is captured through an HSI and a SAR image.

The dataset contains 960×1170 pixel images and five classes, with a spatial resolution of 30 meters. The HSI is acquired by the advanced hyperspectral imager (AHSI) onboard the ZY1-02D satellite, covering 166 bands at 10nm and 20nm spectral resolution. The HSI data were preprocessed by using ENVI software for radiometric and atmospheric correction. The SAR image was captured by the Sentinel-1 satellite. Fig. 8 (c) presents a pseudo-color composite of the HSI and a grayscale LiDAR imagery, accompanied by the ground truth map, while Table 1 shows the sample count for each land-cover class.

4.1.4. LCZ HK dataset (MSI+SAR)

The local climate zone Hong Kong (LCZ HK) dataset [9] offers a comprehensive view of urban and rural areas within Hong Kong, China. It includes multispectral and SAR data, collected by the Sentinel-2 and Sentinel-1 satellites, respectively. The MS images consist of ten spectral bands resampled at 100 meters resolution, while the SAR data are dual-polarized and represented by four components. The spatial size of MSI is 529×528 pixels, and the SAR image is scaled down to the same size. The dataset is categorized into eight distinct land-cover classes as shown in Table 1. Fig. 8 (d) shows pseudo-color composites of the MSI and SAR images, as well as a ground-truth map.

In our experiment, we employ four metrics to quantitatively evaluate the classification performance: class-specific accuracy, overall accuracy (OA), average accuracy (AA), and kappa coefficient (Kappa). These metrics provide comprehensive measures of the classification accuracy.

4.2. Parameter Tuning

The experiments are constructed to analyze the role of main parameters within the S²Fin model. These parameters are local window size and α in Eq. (10), both of which reflect the impact of spatial information on the model. The local window size

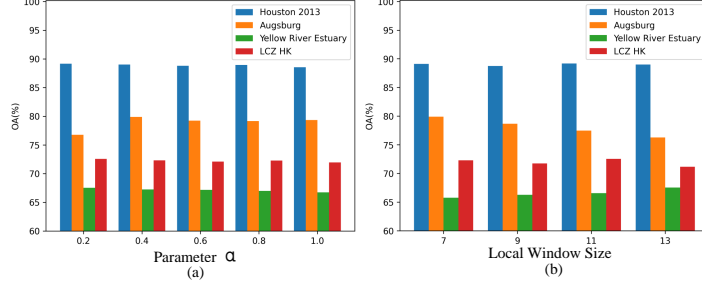


Figure 9: Parameter tuning results on the four datasets. (a) OA (%) with different parameters for α . (b) OA (%) with different local window sizes.

represents the range of spatial information that the network can perceive, while α is a trade-off parameter that determines the spatial amplitude enhancement. To explore the impact of these parameters on the model, we conducted a series of comparative experiments. Specifically, α and local window size are selected from two sets of values $\{0.2, 0.4, 0.6, 0.8, 1.0\}$ and $\{7, 9, 11, 13\}$, respectively.

Table 2: OA (%) with different parameters for α on the four considered datasets

Dataset	0.2	0.4	0.6	0.8	1.0
Houston 2013	89.19	89.02	88.81	88.97	88.56
Augsburg	79.76	79.91	79.23	79.17	79.35
Yellow River Estuary	67.54	67.25	67.18	66.99	66.73
LCZ HK	72.26	72.03	71.80	71.98	71.76

Table 3: OA (%) with different parameters for local window size on the four considered datasets

Dataset	7	9	11	13
Houston 2013	89.10	88.75	89.19	89.02
Augsburg	79.91	78.66	77.47	76.28
Yellow River Estuary	65.78	66.29	66.56	67.54
LCZ HK	72.09	71.54	72.26	70.98

Tables 2-3 illustrate the impact of parameters on the model's performance. Observations from the table reveal that a relatively small value of $\alpha=0.2$ optimizes performance. On the other hand, different datasets have different sensitivities to the local window size. We analyzed and obtained the best parameters for each dataset, which are reported in bold in Table 3. Fig. 9 visualizes the results of parameter tuning.

The experimental framework ¹ is established using PyTorch, executed on an NVIDIA GeForce RTX 3090 24 GB graphics card. The optimization strategy adopted is the adaptive moment estimation (Adam) algorithm, with a learning rate set to 5×10^{-4} and a weight decay of 4×10^{-4} . The learning rate modulation is governed by “MultiStepLR” with a gamma value of 0.5. Furthermore, the trade-off factors α and β are assigned the values of 0.2 and 0.5 respectively. All Mamba blocks are bidirectional with a depth of two. The embedded features have length 64, and training is performed for 320 epochs. The initial trainable spectral high-frequency cutoff threshold is set to 0.5, and the gain coefficient to 0.05. The experiments are performed 10 times and the average value is taken. It is worth noting that in the following comparative experiments, all four datasets use 10 samples per class to represent a condition of few-sample training.

4.3. Ablation Study

To assess the effectiveness of the S²Fin framework, we conduct ablation experiments by systematically removing key modules, including AFCM, HFGM, HFSET, and SSAF. The AFCM employs cosine transformation to enhance high-frequency signals while preserving low-frequency components. The HFGM enhances high-frequency amplitudes to enrich detailed information while the HFSET integrates spectral information from HSI or MSI with spatial features for classification. Lastly, the SSAF module refines the fusion of spatial and spectral features post-frequency processing. The respective experiments in Table 4 are labeled as “AFCM”, “HFGM”, “HFSET” and “SSAF”.

The experimental results are presented in Table 4. In general, removing the spatial-frequency fusion blocks (AFCM and HFGM) leads to lower OA values across all four datasets, indicating their significance to the model. On the other hand, removing

¹All code and implementation details will be made public upon publication.

Table 4: OA (%) obtained in the ablation study on the four considered datasets

Dataset	AFCM	HFGM	HFEST	SSAF	S ² Fin
Houston 2013	88.56	88.41	88.85	89.02	89.19
Yellow River Estuary	67.02	66.54	66.96	67.00	67.56
Augsburg	78.34	77.83	79.88	78.46	79.91
LCZ HK	71.20	71.26	71.60	72.12	72.26

the spatial-spectral fusion block (SSAF) has the least impact on classification performance compared to eliminating other frequency domain components.

4.4. Classification Results

Table 5: Classification results (%) on the Houston2013 dataset with 10 training samples for each class (bold values are the best and underline values are the second)

Class	FusAtNet	AsyFFNet	Fusion-HCT	MACN	CALC	UACL	NCGLF	MSFMamba	S ² Fin
1	80.10	80.10	82.11	96.29	<u>97.99</u>	85.17	96.48	92.25	98.20±1.73
2	85.29	95.82	97.11	<u>97.67</u>	87.22	98.07	82.30	94.28	90.56±4.30
3	83.11	93.30	98.84	99.61	99.13	99.35	<u>99.57</u>	99.56	99.65±0.25
4	87.12	88.01	93.44	96.90	92.79	<u>98.14</u>	95.34	98.94	93.95±2.33
5	<u>99.92</u>	100.00	99.35	97.08	100.00	99.92	99.84	99.22	99.92±0.12
6	84.13	81.90	100.00	98.10	82.54	<u>99.68</u>	84.62	100.00	97.71±1.32
7	83.70	72.97	<u>93.64</u>	85.37	91.02	98.73	81.07	90.84	87.97±4.02
8	67.75	62.64	56.16	62.07	67.75	58.91	70.74	83.65	71.73±5.36
9	<u>81.48</u>	62.88	66.26	72.46	78.58	88.65	78.51	80.47	74.85±3.09
10	40.02	55.46	77.49	<u>78.88</u>	75.35	75.84	86.88	62.93	77.11±5.87
11	87.51	94.61	<u>94.61</u>	94.12	72.33	88.90	94.09	88.39	92.65±4.47
12	31.81	79.31	<u>87.00</u>	73.02	68.77	49.80	75.67	48.85	87.36±4.49
13	89.32	55.34	100.00	<u>95.64</u>	82.79	84.75	93.18	95.18	89.76±1.52
14	100.00	100.00	<u>99.76</u>	95.22	95.93	100.00	97.43	100.00	100.00±0.00
15	91.69	100.00	100.00	100.00	99.69	99.23	100.00	100.00	99.88±0.18
OA	77.09	80.66	87.26	87.54	85.01	86.42	<u>87.83</u>	86.64	89.19±1.06
AA	79.53	81.49	<u>89.72</u>	89.48	86.11	88.34	89.05	89.02	90.75±0.92
Kappa	75.24	79.08	86.26	86.54	83.79	85.33	<u>86.84</u>	85.57	88.31±1.15

Table 6: Classification results (%) on the Augsburg dataset with 10 training samples for each class (bold values are the best and underline values are the second)

Class	FusAtNet	AsyFFNet	Fusion-HCT	MACN	CALC	UACL	NCGLF	MSFMamba	S ² Fin
1	97.79	91.72	92.52	<u>97.83</u>	97.12	94.95	95.30	96.82	98.82±1.59
2	80.95	78.40	79.01	<u>79.04</u>	73.81	69.89	66.22	74.61±3.94	
3	24.99	53.44	40.87	60.90	12.05	42.65	53.91	65.36	60.20±3.70
4	67.12	68.00	70.75	<u>75.99</u>	77.93	79.69	82.34	84.36	82.43±3.42
5	76.46	86.90	90.27	96.70	18.76	93.45	86.61	88.81	97.03±1.23
6	<u>66.79</u>	51.44	68.99	55.66	39.51	49.36	42.25	32.95	36.27±4.66
7	38.03	76.78	62.04	56.38	50.92	<u>72.89</u>	63.20	61.53	63.67±3.85
OA	75.20	75.37	76.18	<u>77.67</u>	76.68	<u>77.56</u>	77.34	77.06	79.91±1.59
AA	64.59	72.39	72.06	73.95	53.62	72.40	70.50	70.86	73.29±0.64
Kappa	67.03	67.53	67.91	<u>70.45</u>	66.87	69.96	70.09	69.67	72.96±1.94

To illustrate the effectiveness of the proposed S²Fin, we have conducted a comparative analysis with seven state-of-the-art multimodal classification models. FusAtNet

Table 7: Classification results (%) on the Yellow River Estuary dataset with 10 training samples for each class (bold values are the best and underline values are the second)

Class	FusAtNet	AsyFFNet	Fusion-HCT	MACN	CALC	UACL	NCGLF	MSFMamba	S ² Fin
1	63.22	<u>87.85</u>	81.07	75.35	68.91	84.78	87.53	90.58	75.71±2.43
2	49.94	53.16	56.53	59.59	85.84	62.74	56.78	65.90	63.45±4.67
3	<u>76.63</u>	59.18	65.15	54.24	25.13	53.37	77.02	46.38	72.64±5.21
4	59.00	54.40	<u>74.85</u>	52.22	53.41	48.08	77.60	66.67	73.52±2.54
5	57.00	48.38	45.72	75.49	19.12	<u>67.40</u>	41.66	48.10	62.89±6.37
OA	57.53	59.56	62.10	62.65	64.60	64.59	64.88	<u>65.34</u>	67.54±2.21
AA	61.09	60.59	64.66	63.38	50.48	63.28	<u>68.12</u>	63.52	69.64±1.97
Kappa	44.26	45.87	49.20	49.37	43.72	51.24	<u>53.02</u>	51.76	55.86±2.52

Table 8: Classification results (%) on the LCZ HK dataset with 10 training samples for each class (bold values are the best and underline values are the second)

Class	FusAtNet	AsyFFNet	Fusion-HCT	MACN	CALC	UACL	NCGLF	MSFMamba	S ² Fin
1	56.52	40.42	41.71	12.72	50.08	45.73	32.69	18.52	<u>52.82±3.99</u>
2	72.78	63.31	<u>74.26</u>	57.40	73.37	68.05	61.54	72.19	76.57±2.32
3	85.44	93.67	74.05	75.63	<u>92.41</u>	67.41	79.43	87.97	80.76±7.03
4	35.75	54.90	51.89	56.86	12.07	52.19	<u>55.35</u>	41.48	38.58±8.34
5	50.00	58.62	73.28	<u>62.93</u>	18.10	44.83	34.48	43.10	52.93±10.24
6	56.36	48.18	60.00	49.09	45.45	<u>63.09</u>	38.18	59.09	66.36±5.92
7	63.78	40.94	69.29	<u>72.44</u>	62.99	65.35	77.17	25.98	32.44±8.05
8	<u>71.77</u>	28.71	46.89	45.93	100.00	69.86	64.11	55.50	66.70±7.71
9	91.34	87.80	83.50	95.39	94.71	69.42	88.79	90.54	86.66±3.22
10	54.72	24.72	65.28	32.08	<u>72.26</u>	77.55	55.28	55.28	66.64±6.98
11	53.30	64.17	94.27	62.85	54.04	54.63	<u>79.30</u>	58.52	69.54±6.86
12	36.36	37.03	17.85	40.16	20.72	40.23	35.08	46.56	40.82±3.52
13	68.11	90.78	<u>94.91</u>	94.99	96.14	97.69	91.86	89.86	92.48±10.58
OA	63.94	68.20	<u>71.87</u>	70.11	69.24	70.34	71.39	68.66	72.26±2.75
AA	61.43	56.40	65.02	58.50	59.75	62.77	61.02	57.28	63.33±1.37
Kappa	59.05	62.15	<u>67.06</u>	64.73	63.80	65.33	66.45	63.27	67.42±2.83

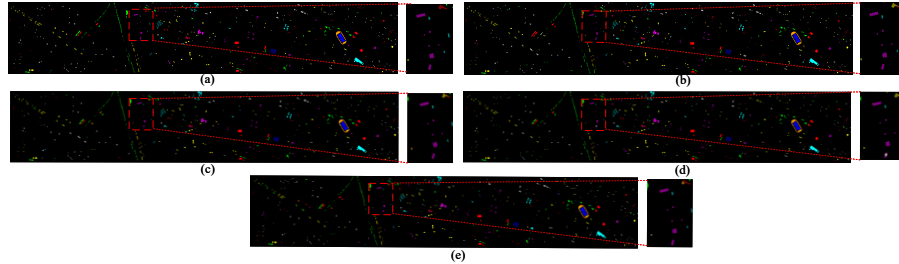


Figure 10: Classification maps and OA% obtained on the Houston 2013 dataset using several methods. (a) Ground-truth map. (b) UACL (86.42%). (c) NCGLF (87.83%). (d) MSFMamba (86.64%). (e) S²Fin (89.19%).

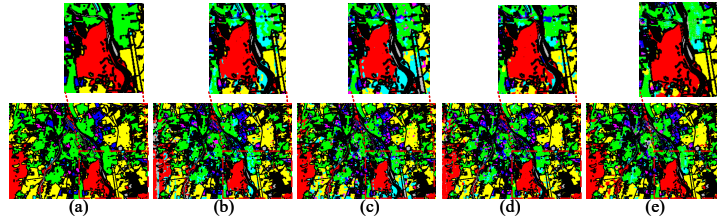


Figure 11: Classification maps and OA% obtained on the Augsburg dataset using several methods. (a) Ground-truth map. (b) UACL (77.56%). (c) NCGLF (77.34%). (d) MSFMamba (77.06%). (e) S²Fin (79.91%).

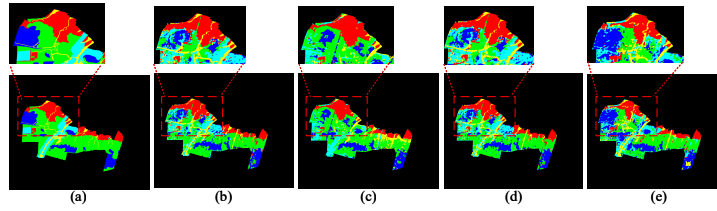


Figure 12: Classification maps and OA% obtained on the Yellow River Estuary dataset using several methods. (a) Ground-truth map. (b) UACL (64.59%). (c) NCGLF (64.88%). (d) MSFMamba (65.34%). (e) S²Fin (67.54%).

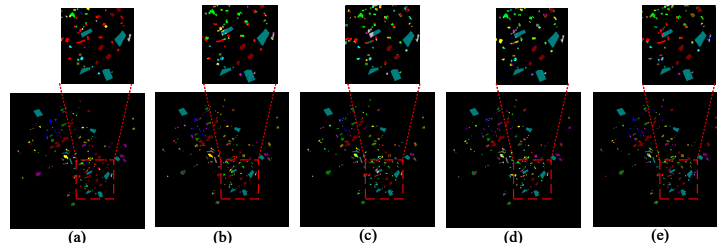


Figure 13: Classification maps and OA% obtained on the LCZ HK dataset using several methods. (a) Ground-truth map. (b) UACL (70.34%). (c) NCGLF (71.39%). (d) MSFMamba (68.66%). (e) S²Fin (72.26%).

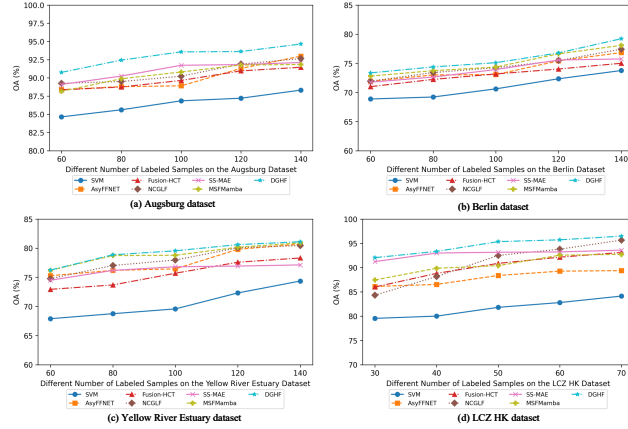


Figure 14: Behaviour of the OA% versus different number of labeled samples on the four considered datasets. (a) Houston 2013 dataset. (b) Augsburg dataset. (c) Yellow River Estuary dataset. (d) LCZ HK dataset.

utilizes a self-attention mechanism to extract spectral features and employs a cross-modality attention mechanism to extract spatial features from multimodal data for land-cover classification. AsyFFNet has crafted an asymmetric neural network with weight-sharing residual blocks for multimodal feature extraction and introduced a channel exchange mechanism and sparse constraints for feature fusion. Furthermore, we have selected five methods that concentrate on global and local multimodal features. Fusion-HCT and MACN integrate CNNs and transformers to capture both local and global features, introducing innovative attention mechanisms for multimodal feature fusion. CALC fuses high-order semantic and complementary information for accurate classification. UACL is based on a contrastive learning strategy to access reliable multimodal samples. NCGLF enhances CNN and transformer structures with structural information learning and invertible neural networks. MSFMamba utilizes multiscale feature fusion state space model to extract multisource information.

The performance of the aforementioned classification methods on the four considered datasets is summarized in Tables 5-8. For a qualitative comparison, the respective classification maps of some methods are depicted in Figs. 10-13. The model is de-

signed to extract fine-grained and discriminative features, so that it can classify better even with a limited number of labeled training samples. To verify the effect of the model under different numbers of training samples, we conducted experiments with 5, 10 and 15 labeled samples for each class. The classification results of each method on the available labeled samples are shown in Fig. 14. Drawing from these outcomes, the following conclusions can be inferred.

1. Overall, advanced approaches which prioritize the integration of global and local features for multimodal data fusion demonstrate excellent classification performance. These approaches tend to outperform those that focus solely on attention mechanisms and network architectures. Meanwhile, these methods exhibit consistent performance across various datasets, attributed to their diverse strategies for fusing global and local information.
2. Leveraging guidance from frequency domain learning, S²Fin has achieved enhanced multimodal feature fusion, reflected in its higher OA, AA, and Kappa scores. Across the four datasets, S²Fin has consistent improvements upon the previous state-of-the-art model by 1.36%, 2.66%, 2.24% and 0.39% on the OA metric. In the few-sample classification scenario, different methods have different sensitivities to the number of labeled samples. S²Fin achieves the best results with 5, 10, and 15 labeled samples per class in all the considered cases.
3. S²Fin emphasis on the high-frequency components of multimodal data enables its effective extraction of details information and classification of complex scenes. For example, from the figures and tables, one can see that on the Augsburg dataset, S²Fin has achieved good classification for 3 out of 7 categories. Notably, the “Forest”, “Low Plants” and “Allotment” classes, which are challenging to distinguish due to their similarities, all achieved commendable classification results. Similarly, on the Houston 2013 dataset, S²Fin has the high classification accuracy in 6 out of the 15 categories, with a good performance

Table 9: Number of parameters (M, million) and GFLOPs of considered methods

		AsyFFNET	CALC	Fusion-HCT	MACN	NCGLF	UACL	MSFMamba	S ² Fin
Augsburg	Params. (M)	1.08	0.94	0.43	0.17	0.44	0.19	0.82	0.63
	GFLOPs	17.76	7.23	0.59	0.70	8.72	2.38	25.17	0.68
Yellow River Estuary	Params. (M)	1.08	0.92	0.43	0.17	0.44	0.18	0.78	0.70
	GFLOPs	17.72	6.80	0.59	0.70	8.72	2.24	25.15	0.99
Houston 2013	Params. (M)	1.08	0.90	0.43	0.17	0.44	0.18	0.97	0.70
	GFLOPs	17.65	6.12	0.59	0.70	8.72	2.01	25.17	0.95
LCZ HK	Params. (M)	1.06	0.79	0.43	0.07	0.34	0.13	0.21	0.65
	GFLOPs	17.32	2.47	0.59	0.37	7.07	0.80	3.83	0.70

in similar “Commercial” and "Residential" class over comparison methods.

4.5. Analysis of the Computational Complexity

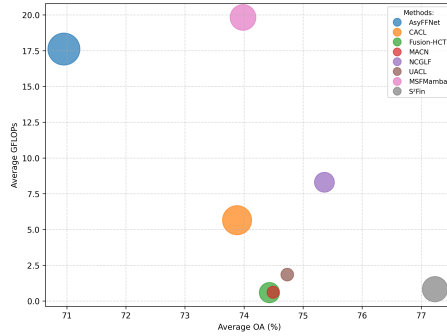


Figure 15: The relationship between the average OA and the average computational complexity (GFLOPs) of different methods.

We evaluate each model’s computational complexity in terms of GFLOPs and parameter count (in millions). Table 9 presents these metrics for the four considered datasets. Fig. 15 shows the relationships between the average (computed on the four datasets) OA and computational complexity (GFLOPs) for the different considered methods. Owing to its minimal number of mamba blocks and a simple yet efficient fusion strategy, our method requires substantially fewer GFLOPs than the mamba-based approach MSFMamba. Furthermore, its number of parameters does not increase significantly with respect to those of other methods and remains lower than those of the AsyFFNET and the CALC. Overall, S²Fin combines low computational complexity with superior classification performance.

5. Conclusion

In this paper, we have proposed S²Fin, a model that integrates frequency domain learning to achieve accurate information extraction and multimodal remote sensing classification with limited labeled samples. S²Fin incorporates the HFSET module, which employs a trainable frequency threshold and a gain factor to amplify critical spectral details, while a two-level spatial-frequency fusion strategy (AFCM and HFRM) combines low-frequency structural features with fine high-frequency details. In addition, SSAF and Mamba blocks consolidate intermediate representations to enhance discrimination.

We first performed ablation experiments to verify the effectiveness of the proposed modules. Besides, we conducted a series of few-sample classification studies on four multimodal datasets, demonstrating that S²Fin achieves superior classification performance with relatively low computational complexity, especially with respect to methods of the same categories. Furthermore, we analyzed the results of S²Fin across different numbers of labeled samples per class, with further confirm the model’s effectiveness.

S²Fin excels at enhancing key features and improving multimodal fusion. However, the potential of Mamba is not fully exploited in this paper. Future research should focus on further integrating frequency domain learning with Mamba structures and fusion modules, as well as exploring more suitable frequency domain learning methods for various multimodal remote sensing applications, such as segmentation and change detection.

CRediT authorship contribution statement

Hao Liu: Conceptualization, Data curation, Formal analysis, Investigation, Methodology, Project administration, Resources, Software, Validation, Visualization, Writing - original draft, Writing – review & editing. **Yunhao Gao:** Conceptualization,

Data curation, Formal analysis, Investigation, Methodology, Resources. **Wei Li:** Conceptualization, Investigation, Visualization, Project administration, Supervision. **Mingyang Zhang:** Formal analysis, Investigation, Methodology, Resources, Writing – review & editing. **Maoguo Gong:** Data curation, Funding acquisition, Investigation, Project administration. **Lorenzo Bruzzone:** Conceptualization, Data curation, Formal analysis, Investigation, Methodology, Project administration, Supervision, Resources, Writing – original draft, Writing – review & editing.

Data availability

The code and data used in this study are available at <https://github.com/HaoLiu-XDU/SSFin>.

Declaration of competing interest

The authors declare that they have no known competing financial interests or personal relationships that could have appeared to influence the work.

Acknowledgements

This work was supported by the China Scholarship Council (Grant No. 202406960026) and the National Natural Science Foundation of China (Grant No. 62376205).

Declaration of generative AI and AI-assisted technologies in the writing process

During the preparation of this work the authors used ChatGPT in order to polish the language. After using this tool, the authors reviewed and edited the content as needed and take full responsibility for the content of the publication.

References

- [1] C. He, B. Gao, Q. Huang, Q. Ma, Y. Dou, Environmental degradation in the urban areas of china: Evidence from multi-source remote sensing data, *Remote Sens. Environ.* 193 (2017) 65–75.
- [2] H. Ye, J. Chang, K. Wang, Z. Jia, W. Sun, Z. Li, A lightweight multilevel multiscale dual-path fusion network for remote sensing semantic segmentation, *Pattern Recognit.* (2025) 112483.
- [3] Y. Gao, X. Song, W. Li, J. Wang, J. He, X. Jiang, Y. Feng, Fusion classification of hsi and msi using a spatial-spectral vision transformer for wetland biodiversity estimation, *Remote Sens.* 14 (4) (2022) 850.
- [4] F. Qingyun, W. Zhaokui, Cross-modality attentive feature fusion for object detection in multispectral remote sensing imagery, *Pattern Recognit.* 130 (2022) 108786.
- [5] W. Li, Y. Gao, M. Zhang, R. Tao, Q. Du, Asymmetric feature fusion network for hyperspectral and sar image classification, *IEEE Trans. Neural Netw. Learn. Syst.* 34 (10) (2023) 8057–8070.
- [6] G. Zhao, Q. Ye, L. Sun, Z. Wu, C. Pan, B. Jeon, Joint classification of hyperspectral and lidar data using a hierarchical cnn and transformer, *IEEE Trans. Geosci. Remote Sens.* 61 (2023) 1–16.
- [7] X. Liu, H. Huo, X. Yang, J. Li, A three-dimensional feature-based fusion strategy for infrared and visible image fusion, *Pattern Recognit.* 157 (2025) 110885.
- [8] T. Wang, G. Chen, X. Zhang, C. Liu, J. Wang, X. Tan, W. Zhou, C. He, Lmfnet: Lightweight multimodal fusion network for high-resolution remote sensing image segmentation, *Pattern Recognit.* 164 (2025) 111579.

[9] D. Hong, L. Gao, N. Yokoya, J. Yao, J. Chanussot, Q. Du, B. Zhang, More diverse means better: Multimodal deep learning meets remote-sensing imagery classification, *IEEE Trans. Geosci. and Remote Sens.* 59 (5) (2021) 4340–4354.

[10] D. Hong, L. Gao, R. Hang, B. Zhang, J. Chanussot, Deep encoder–decoder networks for classification of hyperspectral and lidar data, *IEEE Geosci. Remote Sens. Lett.* 19 (2022) 1–5.

[11] X. Wu, D. Hong, J. Chanussot, Convolutional neural networks for multimodal remote sensing data classification, *IEEE Trans. Geosci. Remote Sens.* 60 (2022) 1–10.

[12] Y. Gao, M. Zhang, W. Li, X. Song, X. Jiang, Y. Ma, Adversarial complementary learning for multisource remote sensing classification, *IEEE Trans. Geosci. Remote Sens.* 61 (Mar.) (2023) 1–13.

[13] J. Wang, W. Li, Y. Wang, R. Tao, Q. Du, Representation-enhanced status replay network for multisource remote-sensing image classification, *IEEE Trans. Neural Netw. Learn. Syst.* (2023) 1–13.

[14] Z. Xue, G. Yang, X. Yu, A. Yu, Y. Guo, B. Liu, J. Zhou, Multimodal self-supervised learning for remote sensing data land cover classification, *Pattern Recognit.* 157 (2025) 110959.

[15] X. Xu, W. Li, Q. Ran, Q. Du, L. Gao, B. Zhang, Multisource remote sensing data classification based on convolutional neural network, *IEEE Trans. Geosci. Remote Sens.* 56 (2) (2018) 937–949.

[16] Z. Xue, X. Tan, X. Yu, B. Liu, A. Yu, P. Zhang, Deep hierarchical vision transformer for hyperspectral and lidar data classification, *IEEE Trans. Image Process.* 31 (2022) 3095–3110.

- [17] J. Lin, F. Gao, X. Shi, J. Dong, Q. Du, Ss-mae: Spatial–spectral masked autoencoder for multisource remote sensing image classification, *IEEE Trans. Geosci. Remote Sens.* 61 (2023) 1–14.
- [18] K. Li, D. Wang, X. Wang, G. Liu, Z. Wu, Q. Wang, Mixing self-attention and convolution: A unified framework for multi-source remote sensing data classification, *IEEE Trans. Geosci. Remote Sens.* 61 (2023) 1–16.
- [19] B. Tu, Q. Ren, J. Li, Z. Cao, Y. Chen, A. Plaza, Ncglf2: Network combining global and local features for fusion of multisource remote sensing data, *Inf. Fusion* 104 (2024) 102192.
- [20] L. Chen, Y. Fu, L. Gu, C. Yan, T. Harada, G. Huang, Frequency-aware feature fusion for dense image prediction, *IEEE Trans. Pattern Anal. Mach. Intell.* 46 (12) (2024) 10763–10780.
- [21] H. Liu, M. Zhang, Z. Di, M. Gong, T. Gao, A. K. Qin, A hybrid multi-task learning network for hyperspectral image classification with few labels, *IEEE Trans. Geosci. Remote Sens.* 62 (2024) 1–16.
- [22] M. S. Pattichis, A. C. Bovik, Analyzing image structure by multidimensional frequency modulation, *IEEE Trans. Pattern Anal. Mach. Intell.* 29 (5) (2007) 753–766.
- [23] T. Qiao, Z. Yang, J. Ren, P. Yuen, H. Zhao, G. Sun, S. Marshall, J. A. Benediktsson, Joint bilateral filtering and spectral similarity-based sparse representation: a generic framework for effective feature extraction and data classification in hyperspectral imaging, *Pattern Recognit.* 77 (2018) 316–328.
- [24] J. Song, A. Sowmya, C. Sun, Efficient frequency feature aggregation transformer for image super-resolution, *Pattern Recognit.* (2025) 111735.

- [25] H. Yu, N. Zheng, M. Zhou, J. Huang, Z. Xiao, F. Zhao, Frequency and spatial dual guidance for image dehazing, in: *Eur. Conf. Comput. Vis.*, 2022, pp. 181–198.
- [26] X. Wu, D. Hong, J. Chanussot, Y. Xu, R. Tao, Y. Wang, Fourier-based rotation-invariant feature boosting: An efficient framework for geospatial object detection, *IEEE Geosci. Remote Sens. Lett.* 17 (2) (2020) 302–306.
- [27] X. Zhao, M. Zhang, R. Tao, W. Li, W. Liao, W. Philips, Multisource remote sensing data classification using fractional fourier transformer, in: *IEEE Geosci. Remote Sens. Symp.*, IEEE, 2022, pp. 823–826.
- [28] R. Tao, X. Zhao, W. Li, H.-C. Li, Q. Du, Hyperspectral anomaly detection by fractional fourier entropy, *IEEE J. Sel. Topics Appl. Earth Observ. Remote Sens.* 12 (12) (2019) 4920–4929.
- [29] X. Zhao, M. Zhang, R. Tao, W. Li, W. Liao, W. Philips, Multisource cross-scene classification using fractional fusion and spatial-spectral domain adaptation, in: *IEEE Geosci. Remote Sens. Symp.*, 2022, pp. 699–702.
- [30] X. Zhao, M. Zhang, R. Tao, W. Li, W. Liao, W. Philips, Cross-domain classification of multisource remote sensing data using fractional fusion and spatial-spectral domain adaptation, *IEEE J. Sel. Topics Appl. Earth Observ. Remote Sens.* 15 (2022) 5721–5733.
- [31] X. Zhao, R. Tao, W. Li, W. Philips, W. Liao, Fractional gabor convolutional network for multisource remote sensing data classification, *IEEE Trans. Geosci. Remote Sens.* 60 (2022) 1–18.
- [32] Y. Sun, Y. Duan, H. Ma, Y. Li, J. Wang, High-frequency and low-frequency dual-channel graph attention network, *Pattern Recognit.* 156 (2024) 110795.

- [33] A. Oppenheim, J. Lim, The importance of phase in signals, *Proc. IEEE* 69 (5) (1981) 529–541.
- [34] K. Xu, M. Qin, F. Sun, Y. Wang, Y.-K. Chen, F. Ren, Learning in the frequency domain, in: *Proc. IEEE Conf. Comput. Vis. Pattern Recognit. (CVPR)*, 2020, pp. 1740–1749.
- [35] H. Sun, Z. Luo, D. Ren, B. Du, L. Chang, J. Wan, Unsupervised multi-branch network with high-frequency enhancement for image dehazing, *Pattern Recognit.* 156 (2024) 110763.
- [36] P. Behjati, P. Rodriguez, C. F. Tena, A. Mehri, F. X. Roca, S. Ozawa, J. Gonzàlez, Frequency-based enhancement network for efficient super-resolution, *IEEE Access* 10 (2022) 57383–57397.
- [37] Y. Wang, Y. Lin, G. Meng, Z. Fu, Y. Dong, L. Fan, H. Yu, X. Ding, Y. Huang, Learning high-frequency feature enhancement and alignment for pan-sharpening, in: *Proc. 31st ACM Int.l Conf. Multimedia*, Oct. 2023, pp. 358–367.
- [38] Y. Zhou, C. Wang, H. Zhang, H. Wang, X. Xi, Z. Yang, M. Du, Tcpsnet: Transformer and cross-pseudo-siamese learning network for classification of multi-source remote sensing images, *Remote Sens.* 16 (17) (2024) 3120.
- [39] K. Ni, D. Wang, Z. Zheng, P. Wang, Mhst: Multiscale head selection transformer for hyperspectral and lidar classification, *IEEE J. Sel. Topics Appl. Earth Observ. Remote Sens.* 17 (2024) 5470–5483.
- [40] X. Xie, Y. Cui, T. Tan, X. Zheng, Z. Yu, Fusionmamba: Dynamic feature enhancement for multimodal image fusion with mamba, *Vis. Intell.* 2 (1) (2024) 37.
- [41] G. Zhang, Z. Zhang, J. Deng, L. Bian, C. Yang, S2crossmamba: Spatial–spectral

cross-mamba for multimodal remote sensing image classification, *IEEE Geosci. Remote Sens. Lett.* 21 (2024) 1–5.

[42] F. Gao, X. Jin, X. Zhou, J. Dong, Q. Du, Msfmamba: Multiscale feature fusion state space model for multisource remote sensing image classification, *IEEE Trans. Geosci. Remote Sens.* 63 (2025) 1–16.

[43] W. Yu, X. Wang, Mambaout: Do we really need mamba for vision?, arXiv preprint arXiv:2405.07992 (2024).

[44] S. Mohla, S. Pande, B. Banerjee, S. Chaudhuri, Fusatnet: Dual attention based spectrospatial multimodal fusion network for hyperspectral and lidar classification, in: *Proc. IEEE Conf. Comput. Vis. Pattern Recognit. Workshops (CVPRW)*, 2020, pp. 92–93.

[45] T. Lu, K. Ding, W. Fu, S. Li, A. Guo, Coupled adversarial learning for fusion classification of hyperspectral and lidar data, *Inf. Fusion* 93 (2023) 118–131.

[46] K. Ding, T. Lu, S. Li, Uncertainty-aware contrastive learning for semi-supervised classification of multimodal remote sensing images, *IEEE Trans. Geosci. Remote Sens.* 62 (2024) 1–13.